

Correction of satellite imagery over mountainous terrain

Rudolf Richter

A method for the radiometric correction of satellite imagery over mountainous terrain has been developed to remove atmospheric and topographic effects. The algorithm accounts for horizontally varying atmospheric conditions and also includes the height dependence of the atmospheric radiance and transmittance functions to simulate the simplified properties of a three-dimensional atmosphere. A database has been compiled that contains the results of radiative transfer calculations (atmospheric transmittance, path radiance, direct and diffuse solar flux) for a wide range of weather conditions. A digital elevation model is used to obtain information about surface elevation, slope, and orientation. Based on the Lambertian assumption the surface reflectance in rugged terrain is calculated for the specified atmospheric conditions. Regions with extreme illumination geometries sensitive to BRDF effects can be optionally processed separately. The method is restricted to high spatial resolution satellite sensors with a small swath angle such as the Landsat thematic mapper and Systeme pour l'Observation de la Terre high resolution visible, since some simplifying assumptions were made to reduce the required image processing time. © 1998 Optical Society of America

OCIS codes: 280.0280, 120.4640, 100.0100.

1. Introduction

The quantitative evaluation of multispectral satellite imagery over mountainous terrain has been an area of research for a number of reasons, e.g., improved land use classification, assessment of erosion hazards, water runoff estimation and resource management, and multitemporal monitoring. The next generation of high spatial resolution satellite sensors such as QUICKBIRD and CARTERRA will provide multispectral and panchromatic imagery of 3–4 m and 1-m resolution, respectively.¹ These products will open exciting new applications in topographic mapping, geographic information systems, urban planning, environmental management, intelligence, and defense. The correction of atmospheric and topographic effects is an important processing step to enhance the data quality, help the interpreter, and improve the performance of subsequent processing, e.g., classification algorithms.

Basically, two different approaches have been used to correct for the varying illumination and reflection geometry caused by the topography. The first employs band ratios² and statistical transformations

such as principal component or regression techniques³ to derive a band-specific and scene-dependent correction. The second approach employs a radiative transfer code to obtain a deterministic description of the correction of topographic effects.^{4–8} The advantage of the second method is that scene-dependent empirical techniques are avoided. The difficulty with this approach is the estimation of radiances, transmittances, and solar fluxes for each image pixel. The model presented here iteratively calculates the ground reflectance in rugged terrain with the Lambertian assumption, i.e., assuming an isotropic reflectance law. Optionally, the last step includes an empirical bidirectional reflectance distribution function (BRDF) correction for regions with extreme illumination geometries employing simple geometric functions. It is an extension to current models, inasmuch as it is capable of deriving two-dimensional (2-D) horizontally varying optical depths and also uses height-resolved atmospheric radiance, transmittance, and solar fluxes to simulate a simplified three-dimensional (3-D) atmosphere. It is an enhancement to the 1996 version of the Atmospheric and Topographic Correction (ATCOR)3 model,⁸ which was restricted to low and medium elevation regions of 0–1.5 km above sea level. Major improvements are the extension of the database, the consideration of radiance reflected from adjacent terrain, which is calculated iteratively, the range dependence of the adjacency effect caused by atmospheric scattering, and special processing for

The author is with the Institute for Optoelectronics, German Aerospace Center, D-82234 Wessling, Germany.

Received 17 July 1997; revised manuscript received 15 January 1998.

0003-6935/98/184004-12\$15.00/0

© 1998 Optical Society of America

low illumination areas. The ATCOR3 model is now applicable in the elevation region from sea level to approximately 4 km.

2. Atmospheric and Topographic Correction Model

The ATCOR3 approach is an extension to the ATCOR2 model with which one can calculate ground reflectance and surface brightness temperature (thermal band) for a flat terrain.^{9,10} Both models utilize the small angle approximation, i.e., the sensor's swath angle is less than $\pm 8^\circ$ with respect to the image center and the solar zenith angle is assumed constant for a recorded scene. Typical representatives of this kind are high spatial resolution satellite sensors such as the Landsat thematic mapper (TM), the Systeme pour l'Observation de la Terre (SPOT) high resolution visible (HRV), and the Indian Remote Sensing Satellite (IRS) with the linear imaging self-scanning (LISS) cameras.¹ Both models are able to handle horizontally varying optical depths and contain a statistical algorithm to remove haze effects.

A radiative transfer code is required to compute the atmospheric transmittance, direct and diffuse solar flux, and path radiance. Here, these quantities are summarized as atmospheric correction functions and they were calculated with the MODTRAN 2 code.¹¹ A database has been compiled for a wide range of typical atmospheric conditions. Subsection 2.A summarizes the scope of the database followed by a presentation of the correction algorithm. The database covers terrain elevations from 0 to 3.5 km above sea level, so satellite images of the elevation regime from 0 to approximately 4 km can be processed.

A. Atmospheric Database

The database contains atmospheric correction functions whose numerical values are stored as look-up tables. They account for the influence of atmospheric absorption and scattering. The main variable atmospheric parameters that affect the radiative transfer in the atmospheric window regions are water vapor content as well as the type of aerosol and the optical depth. The following parameters were explicitly taken into account:

Water vapor content (ground-to-space column): 0.7–4.0-g/cm² range, calculated values are 0.7, 0.8, 1.1, 1.6, 1.7, 2.4, 3.3, 4.0 g/cm² for a ground at sea level.

Aerosol types: rural, urban, maritime, desert.¹²

Visibilities: 5–120 km, calculated values are 5, 7, 10, 15, 23, 40, 80, 120 km.

Ground elevations: 0–3.5 km above sea level, calculated values are 0, 0.5, 1.0, 1.5, 2.0, 2.5 km. Values for the 3- and 3.5-km elevations are obtained by linear extrapolation.

Solar zenith angle: 0–70°, calculated in steps of 10°.

Different view and azimuth angles for tilt sensors.

Interpolated atmospheric functions are provided for intermediate values of zenith angle, ground eleva-

Table 1. Coding of the Optical Depth Channel with the Visibility Index^a

Visibility Index	V (km)	δ
0	180	0.18
1	120	0.20
2	80	0.23
3	55	0.27
4	40	0.32
5	30	0.39
6	23	0.45
7	18	0.51
8	17	0.55
9	15	0.60
10	13	0.66
11	12	0.70
12	11	0.75
13	10	0.80
14	9	0.85
15	8	0.92
16	7	1.01
17	6	1.12
18	5.5	1.20
19	5	1.30
20	4	1.53
21	Haze	
22	Cloud	

^aV is the horizontal visibility, δ is the optical depth at 550 nm, and the ground is at sea level.

tion, and visibility. Table 1 shows the relationship between the horizontal visibility (surface meteorological range) employed by MODTRAN, the optical depth, and the visibility index definition of ATCOR3. A visibility index channel can be optionally appended to the image data after atmospheric correction. The extrapolated visibility ranges from 4 to 180 km.

New atmospheric correction functions can be generated as a linear combination of existing functions. One can save these new look-up tables by assigning a file name, and they are included in the ATCOR3 database, so correction functions can be tuned to weather conditions (radiosonde data, atmospheric transmittance and global flux measurements, fitting water vapor and aerosol, e.g., a mixture of aerosol types with 30% rural and 70% urban).

The look-up tables also depend on the spectral band. Currently, sensors such as the Landsat TM and multispectral scanner, SPOT HRV, IRS LISS, modular optoelectronic scanner-02, EARLYBIRD, QUICKBIRD, and CARTERRA¹ are supported and more than 250,000 table entries have been compiled to cover the above parameter combinations (water vapor, aerosol type, visibility, Sun angle, elevation, view angle) for each spectral band of these sensors.

B. Radiometric Correction Algorithm

For the radiometric correction algorithm, the first step is the interactive masking of haze and cloud areas. Then the reference areas (dense dark vegetation, water surfaces, dark pixels) of known reflec-

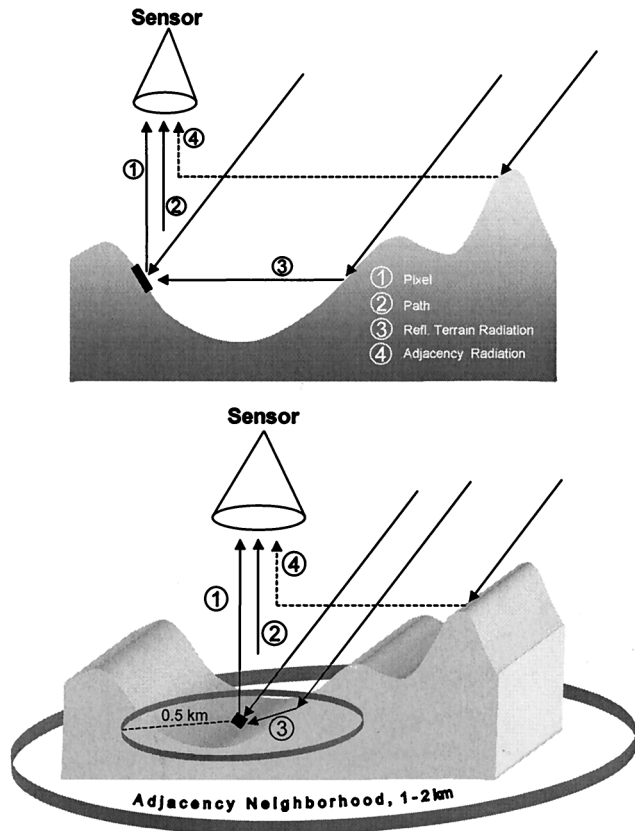


Fig. 1. Radiation components taken into account in the ATCOR3 model.

tance are interactively defined to derive a spatial map of the optical depth.¹³ The reflectance of the reference areas in one spectral band must be specified to calculate the corresponding visibility map.⁹ The visibility index map, compare Table 1, is included as the last channel of the processed image. If the image does not contain a statistically reasonable number of reference pixels, the appropriate visibility can be derived from a stable target of known reflectance or based on typical literature reflectance spectra. In this case a constant visibility in the 5–120-km range must be used for the scene.

Figure 1 shows a schematic sketch of the four radiation components taken into account:

- (1) radiation reflected from the pixel in the instantaneous field of view,
- (2) path radiance,
- (3) reflected terrain radiation from the neighborhood ($R = 0.5$ -km range assumed), and

(4) adjacency radiation caused by atmospheric scattering over adjacent fields of different reflectance (typically the 1–2-km range).

The equations for the first three radiation components are

$$L_1 = \tau_v \frac{\rho}{\pi} (E_{\text{dir}} + E_{\text{dif}}), \quad (1)$$

where τ_v , ρ , E_{dir} , E_{dif} are ground-to-sensor transmittance, ground reflectance, and direct and diffuse solar flux, respectively,

$$L_2 = L_p \quad (\text{path radiance from radiative transfer code}), \quad (2)$$

$$L_3 = \tau_v \frac{\rho}{\pi} \bar{\rho}_{\text{terrain}} E_g, \quad (3)$$

where E_g is the global (direct plus diffuse) flux on the ground. The measured at-sensor radiance L_{sat} can be obtained from the recorded digital number (DN) and the calibration coefficients c_0 , c_1 (Refs. 14 and 15):

$$L_{\text{sat}} = c_0 + c_1 \text{DN}. \quad (4)$$

Neglecting the adjacency component for the moment, one obtains

$$L_{\text{sat}} = c_0 + c_1 \text{DN} = L_1 + L_2 + L_3, \quad (5)$$

from which the following equation can be derived:

$$\rho = \frac{\pi(d^2 L_{\text{sat}} - L_p)}{\tau_v (E_{\text{dir}} + E_{\text{dif}} + \bar{\rho}_{\text{terrain}} E_g)}. \quad (6)$$

Here, the factor d^2 accounts for the current Earth–Sun distance (in astronomical units), since the calculations for the ATCOR3 database were performed with the mean Earth–Sun distance $d = 1$. The final equation has to be extended slightly to account for the directional dependence of the direct and diffuse solar radiation in a rugged terrain. Based on the selected atmosphere (water vapor content, type of aerosol), the visibility map, and the information from the digital elevation model (DEM) resampled to the pixel size of the georeferenced image, the reflectance ρ_i of each pixel is calculated iteratively ($i = 0, 1, 2, 3$) according to

$$\rho_i(x, y) = \frac{\pi\{d^2[c_0 + c_1 \text{DN}(x, y)] - L_p(z)\}}{\tau_v(z)[bE_s \tau_s(z) \cos \beta(x, y) + E_d^*(x, y, z) + E_g(z) \bar{\rho}_{\text{terrain}}^{(i)} V_{\text{terrain}}(x, y)/\pi]}, \quad (7)$$

where the band index is omitted for brevity and the terms are

x, y horizontal coordinates corresponding to the georeferenced pixel positions;

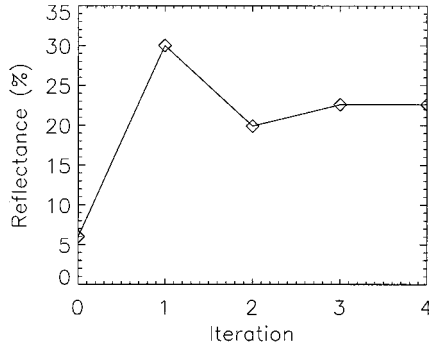


Fig. 2. Influence of the number of iterations on the average terrain reflectance.

- z vertical coordinate containing the elevation information from the DEM;
- DN(x, y) digital number of georeferenced pixel;
- $L_p(z)$ elevation-dependent path radiance;
- $\tau_v(z)$ ground-to-sensor view angle transmittance with direct plus diffuse components;
- $\tau_s(z)$ Sun-to-ground beam (direct) transmittance;
- $\beta(x, y)$ angle between the solar ray and the surface normal (illumination angle);
- b binary factor $b = 1$ if pixel receives direct solar beam, otherwise $b = 0$;
- E_s extraterrestrial solar irradiance;
- $E_d^*(x, y, z)$ diffuse solar flux [see Eq. (8)];
- $E_g(z)$ global flux (direct plus diffuse solar flux on a horizontal surface at elevation z);
- $\bar{\rho}_{\text{terrain}}^{(0)}$ initial value (constant for each band) of average terrain reflectance;
- $\bar{\rho}_{\text{terrain}}^{(i)}(x, y)$ locally varying average terrain reflectance, calculated iteratively ($i = 1, 2, 3$) by low pass filtering the image with a box of $1 \text{ km} \times 1 \text{ km}$, i.e., twice the $R = 0.5\text{-km}$ range;
- $V_{\text{terrain}}(x, y)$ terrain view factor (0–1 range) calculated from the local slope or a horizon analysis.^{7,16,17}

The term $E_s \tau_s(z) \cos \beta(x, y)$ represents the beam irradiance. It is preceded by a binary factor b , where $b = 1$ if direct radiation illuminates pixel (x, y). The factor b is zero if $\cos \beta(x, y) < 0$, which means the pixel is completely in shadow and does not receive direct solar radiation. This applies for the case of self-shadowing. Factor b is also set to zero if shadow is cast from surrounding topography.

Figure 2 demonstrates the rapid convergence of the average terrain reflected radiance with the number of iterations. Results for iteration $i = 4$ deviate less

than 1% from those of iteration $i = 3$, so the number of iterations can be restricted to $i = 3$.

If $\theta_s, \theta_n, \phi_s, \phi_n$ denote solar zenith angle, terrain slope, solar azimuth, and topographic azimuth, respectively, the diffuse solar flux on an inclined plane is calculated with Hay's model¹⁸:

$$E_d^*(x, y, z) = E_d(z) \{ b \tau_s(z) \cos \beta(x, y) / \cos \theta_s + [1 - b \tau_s(z)] V_{\text{sky}}(x, y) \}. \quad (8)$$

Here, $E_d(z)$ is the isotropic diffuse solar flux on a horizontal plane at elevation z . Equation (8) accounts for the anisotropic distribution of the diffuse sky radiance. It is a linear combination of the contribution of the circumsolar diffuse irradiance from the solid angle near the Sun and an isotropic contribution for the remaining sky dome. To assess the influence of the anisotropic diffuse sky radiance there is an option to calculate the isotropic case as well. $V_{\text{sky}}(x, y)$ is the sky view factor (range 0–1).

For the simple trigonometric case one obtains $V_{\text{sky}}(x, y) = \cos^2[\theta_n(x, y)/2]$ based on the local slope angle θ_n . The horizon algorithm provides a more accurate value of the sky view factor by considering the terrain neighborhood of each pixel.^{7,16,17} V_{sky} and V_{terrain} are related by

$$V_{\text{sky}}(x, y) = 1 - V_{\text{terrain}}(x, y). \quad (9)$$

The illumination angle β is calculated from the DEM slope and aspect angles and the solar geometry:

$$\begin{aligned} \cos \beta(x, y) &= \cos \theta_s \cos \theta_n(x, y) \\ &+ \sin \theta_s \sin \theta_n(x, y) \cos[\phi_s - \phi_n(x, y)]. \end{aligned} \quad (10)$$

The next step is the approximate correction of the adjacency effect¹⁹ caused by atmospheric cross talk modifying the radiances of adjacent fields of different reflectances. The final reflectance $\rho_f(x, y)$ depends on the reflectance $\rho(x, y) = \rho_3$ obtained from Eq. (7), step $i = 3$, and the local average reflectance in the neighborhood (typically $1 \text{ km} \times 1 \text{ km}$) of each pixel:

$$\rho_f(x, y) = \rho(x, y) + q[\rho(x, y) - \bar{\rho}(x, y)]. \quad (11)$$

The reflectance difference $\rho(x, y) - \bar{\rho}(x, y)$ is weighted with an atmospheric function q (ratio of diffuse to direct transmittance, also stored in the database⁹), depending on the strength of the atmospheric scattering effect. This equation has been extended to include the range-dependent exponential decrease of the adjacency effect:

$$\begin{aligned} \rho_f(x, y) &= \rho(x, y) + q \left[\rho(x, y) \right. \\ &\quad \left. - \int_0^R \rho(r) A(r) \exp(-r/r_s) dr \right]. \end{aligned} \quad (12)$$

Here, R is the range where the intensity of the adjacency effect has dropped to the 10% level (i.e., $r = R =$

$2.3r_s$, where r_s is a scale range), $\rho(r)$ is the reflectance at range r from the (x, y) position, and $A(r)$ is the area of a circular zone from r to $r + dr$. Usually, R is approximately 0.5–1 km; it could extend to approximately 2–3 km depending on the aerosol height distribution.²⁰ Evaluating Eq. (12) for a sequence of n_R discrete square regions, defined by low pass filtering of the reflectance image $\rho(x, y)$, one obtains

$$\rho_f(x, y) = \rho(x, y) + q \left[\rho(x, y) - \sum_{i=1}^{n_R} \bar{\rho}_i w_i \right], \quad (13)$$

where

$$w_i = \frac{1}{\sum_{i=1}^{n_R} W_i} W_i,$$

$$W_i = \int_{r_{i-1}}^{r_i} A(r) \exp(-r) dr \approx \int_{r_{i-1}}^{r_i} (2r)^2 \exp(-r) dr. \quad (14)$$

The regions extend from r_{i-1} to r_i , where $r_0 = 0$. Since the sequence of moving digital low pass filters works with square filters of size $2r_i \times 2r_i$, the area $A(r)$ is approximated as the corresponding square region $A(r) = (2r)^2$. As an example, for $n_R = 5$ regions the radii were defined as $r_i = (0.45, 0.65, 0.80, 0.90, 1.0) \times R$. The corresponding weight factors are $w_i = (0.24, 0.24, 0.22, 0.15, 0.15)$. The radii were selected such that the first three regions contribute 70% of the total weight, regions 4 and 5 each share 15% of the total weight.

In the special case of an isolated pixel of reflectance ρ surrounded by a uniform background of reflectance ρ_b , Eq. (13) agrees with the simpler Eq. (11), i.e., $\rho_f = \rho + q(\rho - \rho_b)$, and for $\rho_b = \rho$ one obtains $\rho_f = \rho$. So, Eq. (13) fulfills a necessary boundary condition.

C. Areas with Low Illumination: Bidirectional Reflectance Distribution Function Effects

Many surface types exhibit anisotropic reflectance behavior, i.e., the reflectance depends on the viewing and illumination geometry.^{21–23} The relationship is described by the BRDF. An approximation of the BRDF is given by the bidirectional reflectance function, also called biconical reflectance function, which is measured for finite solid angles of incoming and reflected radiation.

For high spatial resolution sensors with a small field of view the solar/viewing geometry is approximately constant in a flat terrain. Therefore, the reflectance image calculated with the assumption of an isotropic (Lambert) reflectance law contains the BRDF properties for this geometry and BRDF variations for a certain cover type because geometry changes are small. However, in mountainous terrain with slopes as large as 30–50° and a solar zenith angle of $\theta_s = 40^\circ$, the range of incident angles will be $\beta = 0-90^\circ$. For this extreme range, most surface types show pronounced anisotropic reflectance properties.

For moderate incident angles $\beta < 60^\circ$, BRDF devi-

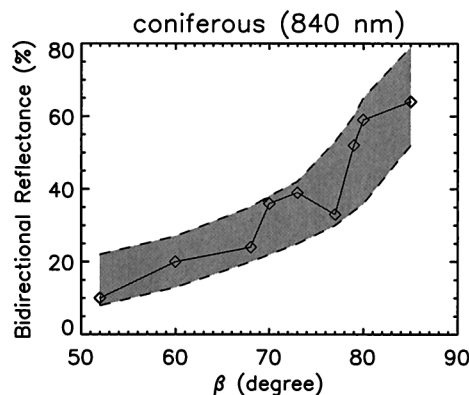


Fig. 3. Bidirectional reflectance of a coniferous forest.

ations from the flat case ($\beta = \theta_s = 40^\circ$) are often less than 30%, whereas for $\beta \approx 70-80^\circ$ deviations might rise to a factor of 2–6.^{21–23} Because of experimental difficulties no field measurements are published in the region $\beta = 80-90^\circ$. There is a further difficulty: in regions of significant slope the BRDF is no longer symmetrical about the principal plane²⁴ and measurements performed on a flat area do not apply. In addition, measurements of tilted natural land surfaces are not available.

Figure 3 shows the bidirectional reflectance of coniferous forest in the near infrared (840 nm). Data were taken from the Landsat TM scene presented in Section 4. The shaded region indicates a typical range of reflectance values, the solid curve corresponds to a certain profile. There is a clear trend of increasing reflectance with rising angle of

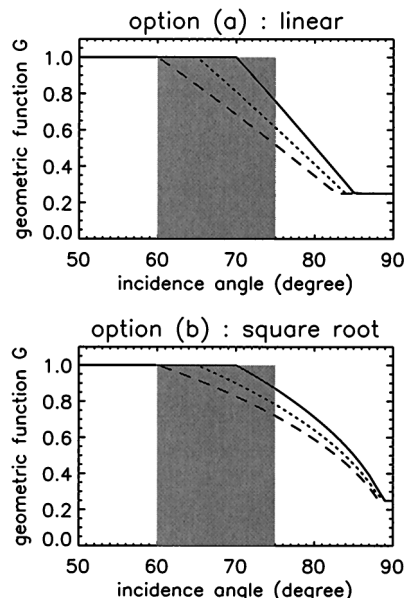


Fig. 4. Geometric function G for options (a) and (b). Threshold angles of 60° , 65° , and 70° are represented by dashed, dotted, and solid curves, respectively, $g = 0.25$. The shaded region indicates the range of incident angles encountered for the selected sample geometry (nadir view, solar zenith angle of 35° , maximum slope of 40°).

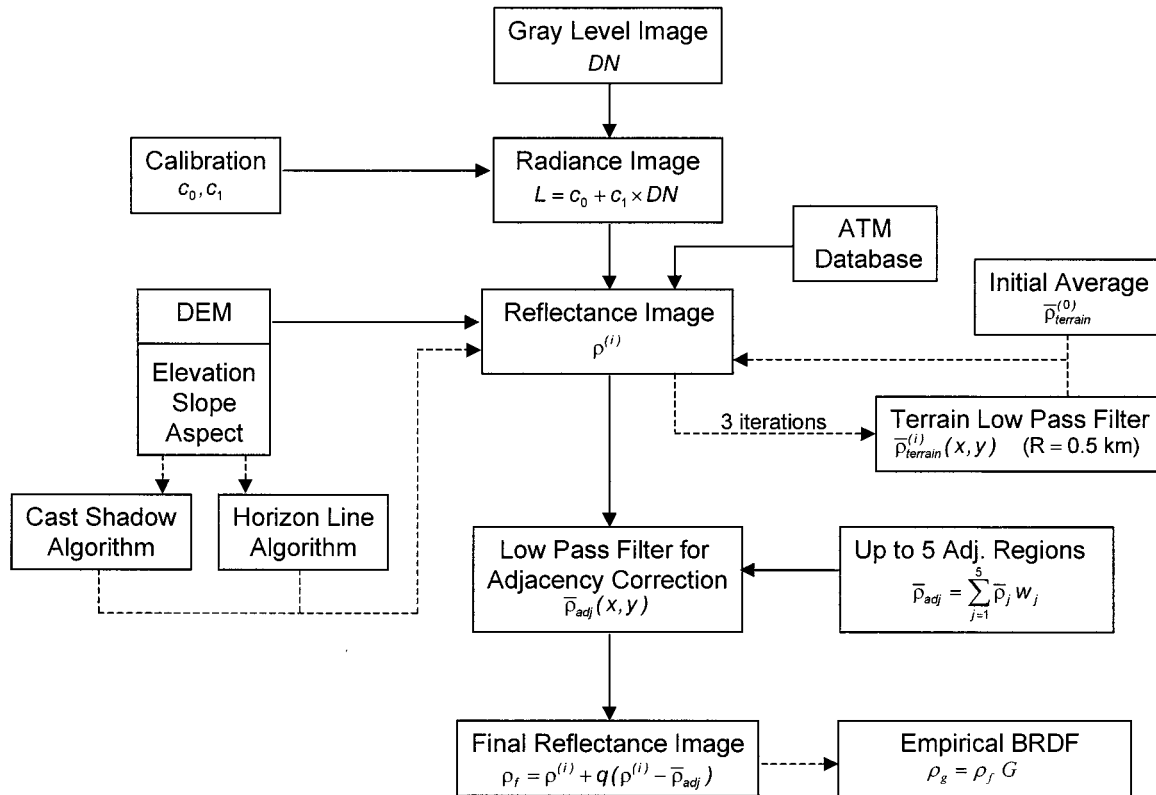


Fig. 5. Block diagram of the main processing steps of the ATCOR3 model.

incidence. Therefore, an empirical approach is optionally offered to process faintly illuminated areas where regions of high reflectance can occur because of BRDF effects.

The following set of empirical functions G [Eqs. (15a)–(15d)] serves to reduce the high reflectance values in regions of extreme geometry to get reflectance values closer to those of adjacent areas with moderate incident angles. G ranges between a specified lower boundary g and 1, i.e., $g \leq G \leq 1$. Only areas of extreme incidence and/or exitance angles are involved, starting with a threshold angle β_T . Values of G greater than 1 are set to 1, and values less than the boundary g are reset to g . This means the processing works in the geometric regime from β_T to 90° . Most of the high spatial resolution satellite sensors have view angles close to nadir, whereas the Sun is usually at a greater distance from nadir. Therefore, the incident angles are more likely to enter the critical region $\beta_i = 60\text{--}90^\circ$ and option (a) or (b) should be applied. Options (c) and (d) also depend on the exitance angle β_e . These options are included for tilt sensors (SPOT, QUICKBIRD, etc.) if scenes are recorded with a larger off-nadir viewing angle (e.g., $20\text{--}30^\circ$), which might be closer to the solar zenith. In this case, the angles β_i and β_e might both enter the critical region $60\text{--}90^\circ$:

$$G = \cos \beta_i / \cos \beta_T, \quad (15a)$$

$$G = (\cos \beta_i / \cos \beta_T)^{1/2} \quad (15b)$$

$$G = \cos \beta_i \cos \beta_e / \cos \beta_T, \quad (15c)$$

$$G = (\cos \beta_i \cos \beta_e / \cos \beta_T)^{1/2}. \quad (15d)$$

The updated reflectance is

$$\rho_g = \rho_f G. \quad (16)$$

Figure 4 shows the course of G for options (a) and (b). The three curves correspond to $\beta_T = 60^\circ, 65^\circ, 70^\circ$ (dashed, dotted, and solid curves, respectively). As an example, for a solar zenith angle of 35° , maximum terrain slope angles of 40° , and a threshold $\beta_T = 60^\circ$, option (a) yields $G = 0.5$, i.e., the reflectance of pixels with incident angles of 75° would be reduced by a factor of 2. Finally, Fig. 5 shows a block diagram of the main processing steps performed by the ATCOR3 model. Solid and dashed lines indicate required and optional processing steps, respectively.

A somewhat different approach exists for low spatial resolution sensors such as the Advanced Very High Resolution Radiometer with which a 3-D model was recently developed.²⁵ The model employs sub-pixel surface cover type information from a digital surface database to generate composite BRDF's for each image pixel to calculate the reflection function of orographically structured landscapes. Because of model complexity and large CPU run times, applications were restricted to very small Advanced Very High Resolution Radiometer subimages of less than 10×10 pixels.

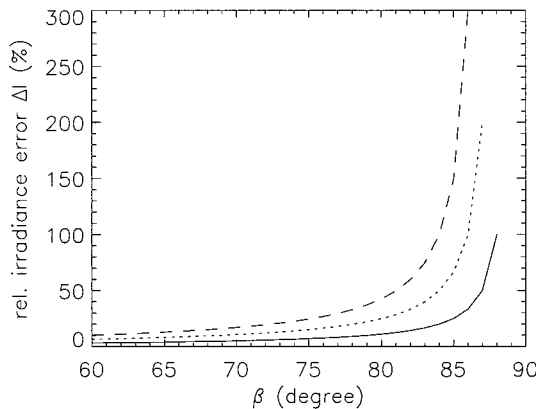


Fig. 6. Relative irradiance error as a function of the solar incident angle β for DEM slope errors $\Delta\alpha = 1^\circ, 2^\circ,$ and 3° (solid, dotted, and dashed curves, respectively) evaluated in the principal plane.

D. Influence of Spatial Resolution of the Digital Evaluation Model

To aggravate BRDF problems the spatial resolution of available DEM's is often not appropriate. The amount of direct solar radiation on a sloped pixel is proportional to the cosine of the illumination angle $[\cos \beta$ of Eq. (7)]. For small to medium incident angles $\beta < 60^\circ$ the cosine function is not sensitive to DEM slope errors. Since areas of low illumination are associated with steep slopes any DEM errors or an inadequate spatial resolution DEM will strongly effect the radiometric processing, compare Figs. 6–8 that show selected examples of the influence of DEM errors on the radiometric signal.

Figure 6 shows the influence of DEM slope errors on the direct irradiance on a sloped surface for solar incident angles of $\beta = 60\text{--}90^\circ$ in the principal plane. For $\beta > 80^\circ$ the relative irradiance error ΔI strongly increases even for small slope errors $\Delta\alpha \leq 3^\circ$, where

$$\Delta I = [\cos \beta / \cos(\beta + \Delta\alpha) - 1] \times 100. \quad (17)$$

Figure 7 presents the corresponding relative reflectance error $\Delta\rho$ for $\beta = 60\text{--}90^\circ$ and a 3° DEM slope error for Landsat TM bands 1, 4, and 7 at 0.48-, 0.84-, and 2.2- μm center wavelengths, respectively. The error $\Delta\rho$ is calculated with an approximation to Eq. (7), neglecting the reflected neighboring terrain radiance and using the local slope angle $\alpha = \theta_n$ for the contribution of the diffuse flux E_{dif} :

$$\Delta\rho = \left\{ \frac{\tau_S E_S \cos \beta + E_{\text{dif}} \cos^2(\alpha/2)}{\tau_S E_S \cos(\beta + 3^\circ) + E_{\text{dif}} \cos^2[(\alpha + 3^\circ)/2]} - 1 \right\} \times 100. \quad (18)$$

The error $\Delta\rho$ is smaller than the ΔI error because of the diffuse flux contribution. $\Delta\rho$ strongly increases with wavelength since the ratio of diffuse to direct flux decreases with wavelength. Figure 8 shows selected examples of the influence of a spatially inadequate DEM and a small amount of misregistration in the subpixel domain. The top is a sketch of the dis-

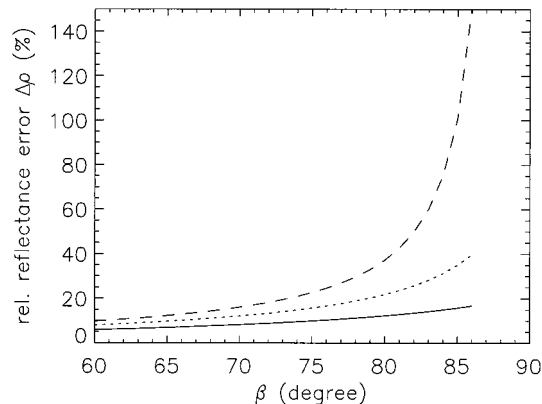


Fig. 7. Influence of a 3° DEM slope error on the reflectance in TM bands 1, 4, and 7 (solid, dotted, and dashed curves, respectively). The simulation parameters are mid-latitude summer atmosphere, rural aerosol, 23-km visibility, 1.5-km ground elevation, solar zenith angle $\theta_S = 40^\circ$, incident angle β in the principal plane, slope angle $\alpha = \theta_n = \beta - \theta_S$.

tribution of different slope elements in an image pixel and defines two configurations. Case 1 considers two subpixel elements of slopes 0° and 45° , each occupying half of the pixel area. Case 2 considers four subpixel slopes $\alpha_i = 30^\circ, 35^\circ, 40^\circ,$ and 45° where each

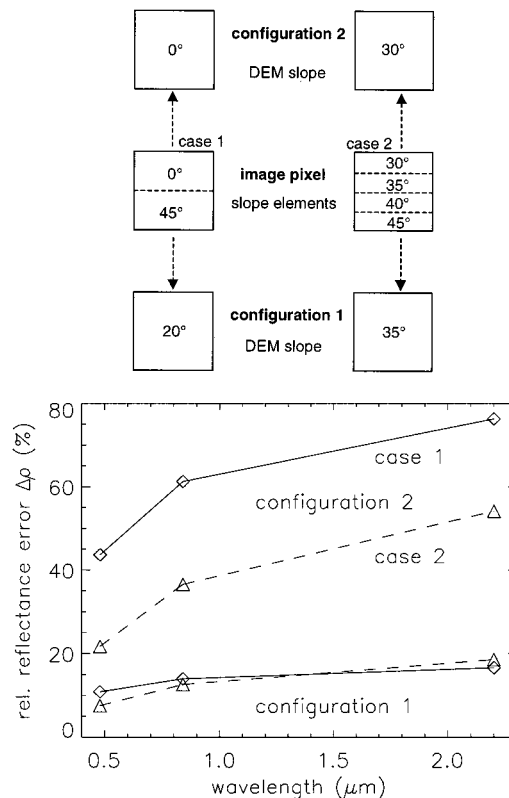


Fig. 8. Influence of a spatially inadequate DEM and a subpixel misregistration. Top, distribution of different slope elements in an image pixel and definition of two configurations. Bottom, relative reflectance error as a function of wavelength. The symbols mark Landsat TM bands 1, 4, and 7. The simulation parameters are the same as in Fig. 4.

slope element occupies a quarter of the pixel area. Configuration 1 replaces the subpixel slope elements by a single DEM slope value ($\alpha = 20^\circ$ and $\alpha = 35^\circ$ for cases 1 and 2, respectively) close to the average slope. Configuration 2 replaces the subpixel elements by the lowest subpixel slope ($\alpha = 0^\circ$ and 30° for cases 1 and 2, respectively). Both configurations represent situations with a small amount of misregistration of 0.25–0.5 pixels (configuration 2) or less (configuration 1) between the DEM resolution cell and a satellite image pixel.

The bottom part of Fig. 8 shows the relative reflectance error $\Delta\rho$ for all the configurations and cases:

$$\Delta\rho = \left\{ \frac{1}{n} \left[\frac{\tau_S E_S \cos \beta + E_{\text{dif}} \cos^2(\alpha/2)}{\sum_{i=1}^n \tau_S E_S \cos \beta_i + E_{\text{dif}} \cos^2(\alpha_i/2)} \right] - 1 \right\} \times 100, \quad (19)$$

where n is the number of slope elements, i.e., $n = 2$ and 4 for cases 1 and 2, respectively. The same geometry and simulation parameters are applied as in Fig. 7, so the solar zenith angle is $\theta_S = 40^\circ$, the incident angle $\beta = \alpha + \theta_S$ is in the principal plane, and $\beta_i = \alpha_i + \theta_S$.

The graphic results indicate that for a homogeneous pixel the errors $\Delta\rho$ are in the 10–20% range if the slope of the DEM resolution cell is close to the average slope of the subpixel elements (configuration 1, both cases). The two curves corresponding to configuration 2 lead to errors of 20–80%. They demonstrate the strong influence subresolution slope surfaces can have on the radiometric signal even if the surface reflectance is homogeneous and the reflectance behavior is isotropic within a pixel.

Inasmuch as the spectral bands of multispectral or hyperspectral sensors are usually coregistered within ± 0.1 to ± 0.25 pixels^{26,27} even a perfect match of the DEM with imagery for a certain band could be associated with a slight mismatch in other bands. So, errors of the magnitude as presented in Figs. 7 and 8 can be expected for geometric situations similar to those discussed here.

3. Discussion

The effects of self-shadowing and shadowing caused by the adjacent topography can be accounted for by resetting the direct solar contribution in Eqs. (7) and (8) to zero ($b = 0$). Self-shadowing can be determined immediately from the solar geometry and the DEM. Topography-induced shadowing requires running a ray-tracing program prior to ATCOR3, the results of which are stored in a binary file with 0 indicating a shadowed pixel and 1 for a nonshadow pixel.

Radiance contributions from surrounding terrain such as reflected radiation from opposite slopes and valleys can be included [term V_{terrain} in Eq. (7)] using the local slope information or the information from a horizon line algorithm.¹⁶ The second option provides more realistic terrain view factors. It is still

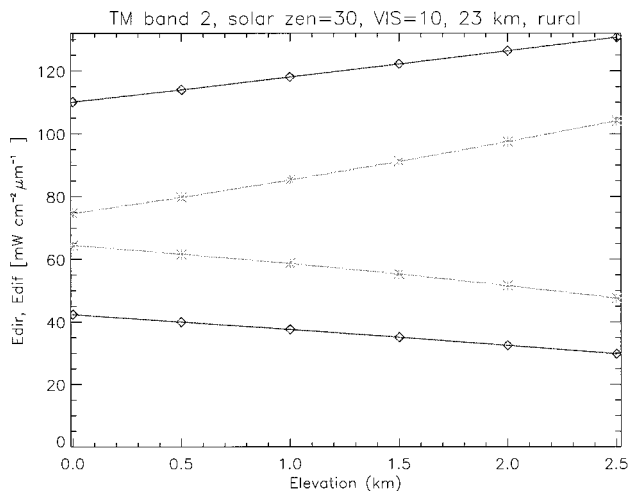


Fig. 9. Direct and diffuse solar fluxes as a function of altitude (ATCOR3 database): diamond, 23-km visibility; asterisk, 10-km visibility. The top line represents the direct solar flux, the lower line the diffuse flux. Mid-latitude summer atmosphere with a rural aerosol and a solar zenith angle of 30° .

an approximation to the real-world situation in rugged terrain, since the reflectance in the neighborhood of each pixel is averaged within a 0.5-km radius. However, it is a reasonable compromise, because the more accurate calculation with pixel-to-pixel view factors weighted with the corresponding single-pixel reflectance leads to prohibitive execution times for large scenes even for the fastest available computers of today.^{25,28}

In addition, the reflected terrain contribution in Eq. (7) neglects the atmospheric attenuation of the path from an opposite slope or valley to the current pixel location. Because of short path lengths of less than 0.5 km, this approximation is acceptable but leads to a small overestimation of this radiance component.

Figure 9 shows the direct and diffuse fluxes as a function of terrain elevation for a selected cloud-free standard atmosphere. The database contains calculations for the 0–2.5-km elevation range, in steps of 0.5 km. Because of the linear behavior of these functions, values for the 3- and 3.5-km elevations can be obtained by linear extrapolation with an error of less than 5%. To obtain a fast image processing algorithm, the height-dependent functions are interpolated to a 100-m grid, and each image pixel is put into the appropriate class for the nearest 100-m grid point. Errors that are due to this approximation are of the order of 2%. The extrapolation and interpolation errors are tolerable, since in most cases atmospheric parameters are not available and must be estimated from the image data itself.

The most critical points for the radiometric correction are bidirectional reflectance effects, the spatial resolution of the DEM,²⁹ and the calculation of slope and aspect from digital terrain data.³⁰ Artifacts might arise when the DEM resolution cell is not adequate for the pixel size of the imaging satellite sensor. It would be desirable to have a spatial res-

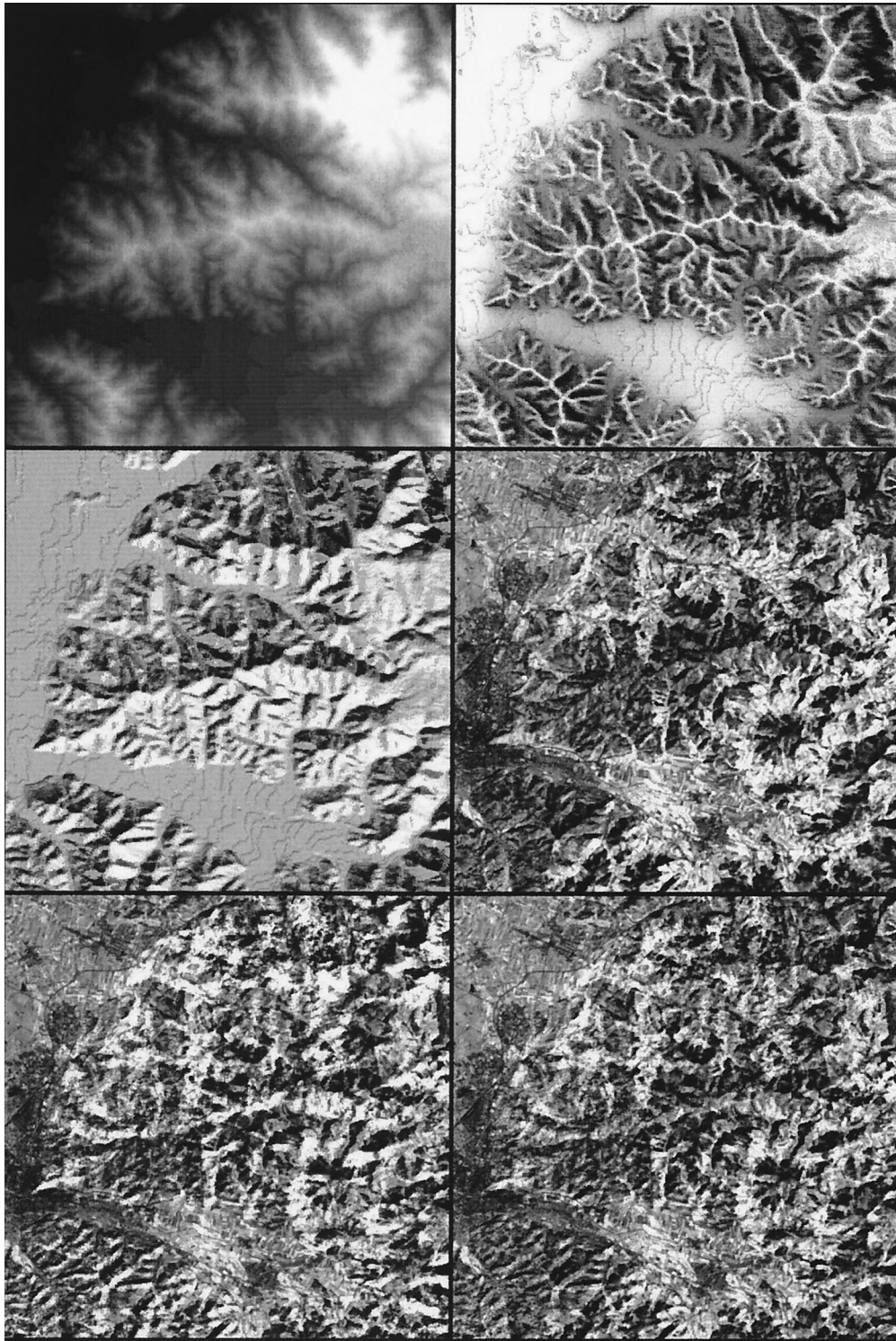


Fig. 10. Digital elevation image and Landsat TM band 4 images, see text. Top, DEM (left), sky view factor (right); middle, illumination image (left), original TM band 4 image (right); bottom, reflectance images without (left) and with separate processing of low illumination areas (right).

olution of 0.25 times the pixel size or better.²⁹ In terms of the Landsat TM this would require DEM data, with approximately 7-m resolution, for the 10-m SPOT panchromatic imagery DEM's with 2.5 m, and for the 1-m panchromatic QUICKBIRD and CARTERRA data the DEM resolution would

have to be 0.25 m. For most areas of the world such high spatial resolution data are not available. Even though they may exist for some areas or will be generated in the future, there will always be a trade-off with price, so in most cases lower resolution DEM's in the 10–100-m range have to be used.

4. Sample Case

Here the selected results for a 500×500 pixel subscene of the Landsat-5 TM are presented. The acquisition date of the scene is 12 September 1985 (path 195/row 27). The $15 \text{ km} \times 15 \text{ km}$ area covers part of the Black Forest (Germany) and consists mainly of coniferous and deciduous forests, meadows, and some villages. The solar zenith angle is 49° , the azimuth angle is 146° . The TM subscene was georeferenced with respect to a topographic map using seven ground control points and a bilinear interpolation algorithm.

A DEM with a spatial resolution of $50 \text{ m} \times 50 \text{ m}$ calculated from digitized contour lines was resampled to $30 \text{ m} \times 30 \text{ m}$ to match the TM pixel size (DEM release approved 15 January 1997, Az. 4.3/279, State Authority Landesvermessungsamt Baden-Württemberg, Stuttgart, Germany). The ERDAS, Inc. topographic module³¹ was employed to generate the slope and aspect images. The elevation range of the selected image is 100 m (dark areas, top left of elevation image of Fig. 10) to approximately 1300 m (bright areas). The top right image presents the sky view factor calculated with the horizon line algorithm¹⁶ using 32 azimuth directions. Bright areas indicate a high sky view factor (flat regions and mountain ridges), dark areas indicate a low value (in the valleys). The middle section of Fig. 10 shows the illumination conditions ($\cos \beta$) for each pixel, bright and dark areas present a small and a large solar incident angle, respectively. To the right, the original TM band 4 (760–900-nm) scene is displayed. The two bottom images of Fig. 10 show the results with combined atmospheric/topographic correction (left, isotropic reflectance law; right, empirical BRDF correction for areas of low illumination). After topographic correction the illumination effect is strongly reduced causing the impression of a flat terrain. For incident angles of $70\text{--}90^\circ$ some areas of high reflectance values appear. In the bottom right image, the empirical BRDF option is employed [Eq. (15a)] with a threshold angle of 65° and a lower bound of $g = 0.33$. Most of the bright patches now have reflectance values closer to those of neighboring areas with moderate solar incident angles ($30\text{--}60^\circ$). Figure 11 presents a spectrum of coniferous forest for a slope angle of 30° facing the Sun. The solid curve indicates the combined atmospheric/topographic correction, the dashed curve indicates atmospheric correction only. When the topographic correction is neglected, the reflectance of surfaces that face the Sun is overestimated and is underestimated for surfaces oriented away from the Sun. The effect is most pronounced in spectral bands with high target reflectance values.

A validation of the results in the strict sense of a comparison of model results with ground measurements of different surface types for a range of terrain slopes, aspects, and illumination conditions would be a huge logistic and financial effort and is currently not available. In addition, one of the common tech-

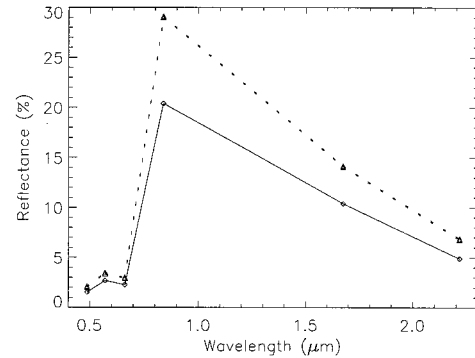


Fig. 11. Coniferous spectrum: solid curve, atmospheric and topographic correction, slope of 30° , aspect to Sun; dashed curve, only atmospheric correction.

niques of deriving atmospheric parameters, the Langley method,³² is often not applicable, because the terrain might block the direct solar beam for the important regime of low Sun elevations. Therefore, a validation can be performed only on a statistical basis, and Fig. 12 presents an example of a regression analysis of TM band 4 data for coniferous forest areas. The top graph indicates the correlation of the TM band 4 reflectance with the illumination angle $\cos \beta$, neglecting the topographic influence. A significant correlation coefficient of 0.84 is obtained, i.e.,

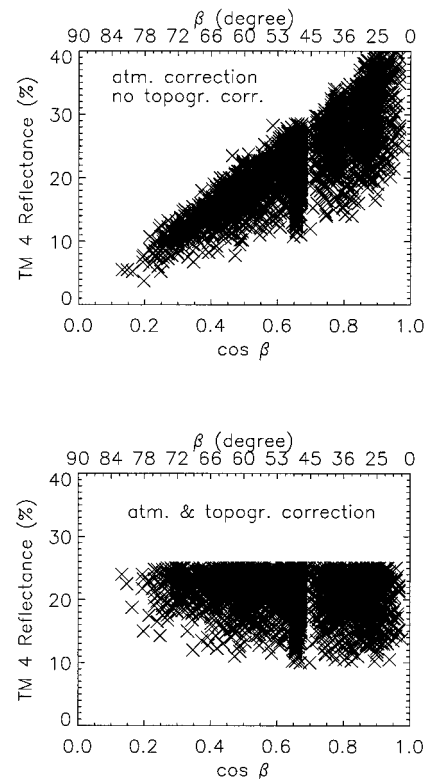


Fig. 12. Regression analysis for TM band 4 data of a coniferous forest. The reflectance values in the bottom graph were cut at the 10% and 25% reflectance levels to separate the coniferous forest from other vegetation cover types.

small illumination angles ($\cos \beta > 0.8$) cause high radiance values and are interpreted as high reflectance, and large illumination angles ($\cos \beta < 0.4$) cause a low signal at the sensor that is interpreted as a low reflectance. The bottom graph shows the results when the topographic effect is taken into account. A substantially reduced correlation coefficient of 0.18 is obtained in this case, demonstrating the successful removal of topographically induced illumination conditions.

5. Conclusions

A number of simplifications were used in this approach to achieve the objective of a fast image processing algorithm for the correction of radiometric effects over rugged terrain. First, the method neglects variations of the sensor view angle and Sun angle within the scene, so it is restricted to small field-of-view instruments. Second, it works only for the cloud-free parts of imagery; cloud and cloud-shadow effects are not taken into account. Third, it uses a large database of elevation-dependent correction functions for a wide range of standard atmospheres, with interpolated values on a 100-m grid. Finally, radiance contributions reflected from neighboring terrain are included with a simple spatial average. Last but not least, there is an option to correct empirically areas of high reflectance values caused by bidirectional reflectance behavior at extreme viewing or illumination geometries.

The resulting execution time for an image of 1000×1000 pixels is approximately 1 min/spectral band on a typical workstation (IBM RS/6000-580), which is a factor of 8 slower than for the corresponding ATCOR2 algorithm working in flat terrain. This is due mainly to the three iterations for the reflected neighboring terrain radiation. Without terrain iterations the difference in execution time between both models is approximately a factor of 3.

A quantitative assessment of the model accuracy is difficult, since the results depend on a number of parameters that are usually not accurately known, such as atmospheric conditions and bidirectional surface reflectances, or that have to be accepted, such as a coarse DEM resolution. However, the method worked well in different projects ranging from forest applications to the geology of desert sand surfaces, and successfully compensated topography-induced effects. It might also produce artifacts, especially in areas of low Sun illumination and along mountain ridges. A look at the illumination image derived from the DEM then helps to interpret these artifacts. In many cases, they are caused by an inadequate spatial resolution of the DEM.

References

1. M. D. Keister, project ed., *Multispectral Imagery Reference Guide* (Logicon Geodynamics, Fairfax, Va., 1997).
2. B. N. Holben and C. O. Justice, "The topographic effect on spectral response from nadir-pointing sensors," *Photogr. Eng. Remote Sensing* **46**, 1191–1200 (1980).
3. D. L. Civco, "Topographic normalization of Landsat Thematic

- Mapper digital imagery," *Photogr. Eng. Remote Sensing* **55**, 1303–1309 (1989).
4. R. W. Sjöberg and B. K. P. Horn, "Atmospheric effects in satellite imaging of mountainous terrain," *Appl. Opt.* **22**, 1701–1716 (1983).
5. C. Conese, M. A. Gilabert, F. Maselli, and L. Bottai, "Topographic normalization of TM scenes through the use of an atmospheric correction method and digital terrain models," *Photogr. Eng. Remote Sensing* **59**, 1745–1753 (1993).
6. C. Proy, D. Tanre, and P. Y. Deschamps, "Evaluation of topographic effects in remotely sensed data," *Remote Sensing Environ.* **30**, 21–32 (1989).
7. S. Sandmeier and K. I. Itten, "A physically-based model to correct atmospheric and illumination effects in optical satellite data of rugged terrain," *IEEE Trans. Geosci. Remote Sensing* **35**, 708–717 (1997).
8. R. Richter, "Correction of atmospheric and topographic effects for high spatial resolution satellite imagery," *Int. J. Remote Sensing* **18**, 1099–1111 (1997).
9. R. Richter, "A spatially adaptive fast atmospheric correction algorithm," *Int. J. Remote Sensing* **17**, 1201–1214 (1996).
10. R. Richter, "Atmospheric correction of satellite data with haze removal including a haze/clear transition region," *Comput. Geosci.* **22**, 675–681 (1996).
11. A. Berk, L. S. Bernstein, and D. C. Robertson, "MODTRAN: a moderate resolution model for LOWTRAN 7," GL-TR-89-0122 (U.S. Air Force Geophysics Laboratory, Hanscom Air Force Base, Mass., 1989).
12. E. P. Shettle and R. W. Fenn, "Models of the aerosols of the lower atmosphere and the effects of humidity variations on their optical properties," AFGL-TR-79-0214 (U.S. Air Force Geophysics Laboratory, Hanscom Air Force Base, Mass., 1979).
13. Y. J. Kaufman and C. Sendra, "Algorithm for automatic atmospheric corrections to visible and near-IR satellite imagery," *Int. J. Remote Sensing* **9**, 1357–1381 (1988).
14. P. N. Slater, S. F. Bigyar, R. G. Holm, R. D. Jackson, Y. Mao, J. M. Palmer, and B. Yuan, "Reflectance and radiance-based methods for the in-flight absolute calibration of multispectral sensors," *Remote Sensing Environ.* **22**, 11–37 (1987).
15. J. C. Price, "Calibration comparison for the Landsat 4 and 5 multispectral scanners and thematic mappers," *Appl. Opt.* **28**, 465–471 (1989).
16. J. Dozier, J. Bruno, and P. Downey, "A faster solution to the horizon problem," *Comput. Geosci.* **7**, 145–151 (1981).
17. J. Hill, W. Mehl, and V. Radeloff, "Improved forest mapping by combining corrections of atmospheric and topographic effects in Landsat TM imagery," in *Sensors and Environmental Applications of Remote Sensing*, J. Askne, ed. (Balkema, Rotterdam, The Netherlands, 1995).
18. J. E. Hay and D. C. McKay, "Estimating solar irradiance on inclined surfaces: a review and assessment of methodologies," *Int. J. Sol. Energy* **3**, 203–240 (1985).
19. J. V. Dave, "Effect of atmospheric conditions on remote sensing of a surface nonhomogeneity," *Photogr. Eng. Remote Sensing* **46**, 1173–1180 (1980).
20. Y. J. Kaufman, "Atmospheric effect on spatial resolution of surface imagery," *Appl. Opt.* **23**, 3400–3408 (1984).
21. K. T. Kriebel, "Measured spectral bidirectional reflection properties of four vegetated surfaces," *Appl. Opt.* **17**, 253–259 (1978).
22. D. S. Kimes, "Dynamics of directional reflectance factor distributions for vegetated canopies," *Appl. Opt.* **22**, 1364–1372 (1983).
23. D. W. Deering, T. F. Eck, and J. Otterman, "Bidirectional reflectances of selected desert surfaces and their three-parameter soil characterisation," *Agri. Forest Meteorol.* **52**, 71–93 (1990).

24. B. C. Schaaf, X. Li, and A. H. Strahler, "Topographic effects on bidirectional and hemispherical reflectances calculated with a geometric-optical canopy model," *IEEE Trans. Geosci. Remote Sensing* **32**, 1186–1193 (1994).
25. W. Thomas, "A three-dimensional model for calculating the reflection functions of inhomogeneous and orographically structured natural landscapes," *Remote Sensing Environ.* **59**, 44–63 (1997).
26. J. L. Engel and O. Weinstein, "The Thematic Mapper - an overview," *IEEE Trans. Geosci. Remote Sensing* **21**, 258–265 (1983).
27. S. Kalyanaraman, R. K. Rajangam, and R. Rattan, "Indian remote sensing spacecraft 1C/1D," *Int. J. Remote Sensing* **6**, 791–799 (1995).
28. C. C. Borel, S. A. Gerstl, and B. J. Powers, "The radiosity method in optical remote sensing of structured 3-D surfaces," *Remote Sensing Environ.* **36**, 13–44 (1991).
29. D. G. Goodenough, J. C. Deguise, and M. A. Robson., "Multiple expert systems for using digital terrain models," in *Proceedings of the International Geoscience and Remote Sensing Symposium*, R. Mills, ed. (Institute of Electrical and Electronic Engineers, Washington, D.C., 1990), p. 961.
30. J. R. Carter, "The effect of data precision on the calculation of slope and aspect using gridded DEMs," *Cartographica* **29**, 22–34 (1992).
31. ERDAS Field Guide, 2nd ed., version 7.5, (ERDAS, Inc., Atlanta, Ga., 1991), pp. 169–190.
32. P. N. Slater, *Remote Sensing: Optics and Optical Systems* (Addison-Wesley, Reading, Mass., 1980).